Pergamon

Acta mater. Vol. 47, No. 1, pp. 149–164, 1999
Acta Metallurgica Inc.
Published by Elsevier Science Ltd
Printed in Great Britain
1359-6454/99 $19.00 + 0.00

PII: S1359-6454(98)00327-9

CREEP BEHAVIOR OF INTERFACES IN FIBER REINFORCED METAL–MATRIX COMPOSITES

J. V. FUNN and I. DUTTA†

Center for Materials Science and Engineering, Department of Mechanical Engineering, Naval Postgraduate School, Monterey, CA 93943, U.S.A.

(Received 2 June 1998; accepted 9 September 1998)

Abstract—The elevated temperature deformation behavior of interfaces in model single fiber composites was isolated and studied using a fiber push-down approach, whereby the interface is loaded in shear. Two fiber–matrix systems, one with no mutual solubility (quartz–lead) and the other with limited mutual solubility (nickel–lead), were investigated. In both systems, the matrix and fiber underwent sliding relative to each other, with the interface acting as a high diffusivity path. The mechanism of sliding was inferred to be interface-diffusion-controlled diffusional creep with a threshold stress (Bingham flow). The behavior was modeled analytically using a continuum approach, and an expression for the constitutive creep behavior of the interface was derived. The model provided a physical basis for the observed threshold behavior, which was found to be directly related to the normal (radial) residual stress acting on the fiber–matrix interface. The results are deemed to be significant because: (1) in some instances, interfacial sliding may be instrumental in determining the overall creep/thermal cycling response of a composite; and (2) they offer an alternative rationalization of threshold behavior during diffusional flow (besides interface reaction control) and may be useful in understanding creep in multi-phase systems with internal stresses. *Acta Metallurgica Inc. Published by Elsevier Science Ltd*

1. INTRODUCTION

It is well known that continuous fiber reinforced metal–matrix composites display significantly better creep resistance and stress rupture life than the corresponding unreinforced matrix alloy [1–15]. In general, it is believed that during isothermal creep at constant applied load, the matrix undergoes stress relaxation, the relaxed stress being transferred to the fibers. Since the fibers are typically much stiffer, stronger and more refractory (i.e. more creep resistant) than the matrix, this gives rise to a gradually decreasing creep rate when a continuous fiber composite is subjected to a constant stress creep test [8, 9]. Eventually, one of two things can happen. If the applied stress is relatively low, all of the stress is supported by the fibers, and the composite creep rate becomes equal to zero for non-creeping fibers, or to the creep rate of the fibers for creeping fibers. If on the other hand, the applied stress is large, the fibers are progressively loaded due to matrix stress relaxation till the fracture strength of some of the fibers is reached, at which point, the fibers start failing and the composite creep rate increases again till failure occurs [8, 9, 13].

While the above micro-mechanical representation of creep is generally agreed upon, the role of interfaces on creep in composites is a subject of significant confusion, despite having been considered in a number of studies [13, 14, 16–21]. Although continuous fiber reinforced composites are generally thought to deform with the matrix and fiber in iso-strain condition, there is ample evidence in the literature that this condition is often violated, even in the absence of interfacial fracture. This is most clearly observed following thermal cycling of composites in the absence of any applied load [22, 23]. For instance, Yoda *et al.* [22] observed that the ends of W fibers in a Cu matrix intruded into the matrix following thermal cycling, the extent of intrusion increasing with increasing number of cycles. Similar effects have been observed following *slow* thermal cycling of graphite fiber reinforced aluminum composites [23], whereupon the matrix was observed to protrude past the fiber ends. In both cases [22, 23], the slow heating/cooling rates during cycling, in conjunction with the tensile matrix residual stress along the fiber-axes, allowed the matrix to *elongate* relative to the fibers via creep. Here, no interfacial debonding occurs, and the differential strain between the matrix and fibers is accommodated by *time-dependent diffusional sliding* at the interface close to fiber-ends, where large interfacial shear stresses exist. This is very different from the effect observed during relatively *rapid* thermal cycling, where interfacial fracture, followed by *frictional sliding* at the debonded interface, results in the relief of axial tensile residual stresses in the matrix, allowing the matrix to *shrink* relative to the fibers [24, 25]. Fricitonal sliding is commonly

†To whom all correspondence should be addressed.

observed in composites with weak interfaces which undergo debonding during cycling [24–26], whereas time-dependent sliding via interfacial creep occurs in the absence of debonding [22, 23]. Indirect evidence of interfacial sliding during isothermal creep has been noted in γ-TiAl reinforced by Ti_2AlC platelets, where, beyond about 60 percent of the melting temperature, the composite creep strength was observed to decrease below that of the unreinforced matrix, despite the absence of any interfacial debonding or fracture [27]. This loss of strength at high temperatures has been attributed to diffusional relaxation of the matrix, accommodated by diffusionally accommodated sliding at the interface [19].

Broadly, the interfacial contribution to creep has been thought of in two different ways. In the first case, the "interface" is thought to consist of a highly dislocated region of the matrix (a work hardened zone), formed due to the higher elastic modulus of the fiber relative to the matrix, which makes matrix dislocation loops moving towards the fiber stand off at some equilibrium distance from the fiber [18, 13, 14]. This is followed by recovery processes driven either by dislocation annihilation processes in the work hardened zone [18], or by the non-conservative glide of prismatic loops along the interface [13, 14]. Both allow the interface to accommodate differential strain rates between the matrix and fiber. This type of behavior may be represented by a power-law creeping interfacial region, which has been the basis for a number of models proposed in the literature [14, 16–18].

An alternative treatment considers the interface as being able to deform via two independent but related mechanisms [20, 21, 28]. First, the interface is thought to slide in shear with a linear rheology, e.g. due to the presence of an interphase layer creeping in the diffusional creep regime. Secondly, mass transport by short range interfacial diffusion, driven by gradients in the interfacial normal or hydrostatic stress state due to the presence of interfacial asperities, is also considered to be possible. Analyses suggest that both mechanisms (i.e. diffusive transport and interface sliding with a linear rheology) have a similar effect on the deformation behavior of the composite [20]. Further, since both diffusional flow and viscous drag have the same linear stress dependence, and the same direction of net flow, it is possible that interfacial flow may be governed by a single constitutive law that combines the effects of both normal and shear stresses at the interface.

To date, no direct experimental verification of the strain rate–stress relationship governing interfacial creep has been reported. The only methodology for obtaining insight into the interfacial deformation mechanism has consisted of assuming an interfacial flow law, followed by modeling of the deformation behavior of the entire composite using this flow law and then comparing the analytical/numerical results with experiments based on a real composite system [17–20, 28]. However, because of the complex nature of a real composite *vis-à-vis* (i) the alignment and distribution of fibers, (ii) the interfacial stresses of both applied and residual origins, (iii) the precise chemistry/nature of the interfacial region, and (iv) the concurrent operation of multiple deformation mechanisms, an accurate description of the phenomenology of interfacial sliding is difficult to ascertain using the above methodology.

Accordingly, the purpose of this paper is twofold. The first goal is to design and conduct experiments on a model single fiber composite with the purpose of isolating and studying interfacial deformation without being influenced by mechanisms associated with the matrix. And secondly, based on the experimental results, we aim to develop an explicit constitutive law for interfacial sliding in a fibrous composite in the absence of interface fracture.

2. APPROACH

Two model single fiber composite (SFC) systems, both based on a lead matrix of 99.99% purity, were chosen for the present experiments. Quartz or nickel (work hardened to a yield strength of 500 MPa) fibers of 0.001 m nominal diameter (d_{fiber}) were chosen as the reinforcement. Both quartz and nickel show good wetting by lead, and therefore provided well-bonded interfaces without any discontinuity. Quartz and Pb have negligible mutual solubility at or below the melting temperature of lead, and therefore the quartz–Pb SFC represents a system with a "sharp" interface. Contrarily, the solubility limit of Pb in Ni at 473 K is about 1 wt% (although there is no solubility of Ni in lead) [29], and therefore this system has a relatively "diffuse" interface.

The composites were fabricated by first melting lead in a test tube located inside a crucible furnace at 798 K under an inert gas (argon) cover, and then inserting a single fiber (quartz or Ni) into the test tube using a special fixture in order to ensure accurate alignment of the fiber and test tube axes. Following fiber insertion, the exposed surface of the composite was immediately covered by graphite powder to minimize oxidation, and a thick layer of alumina powder to reduce temperature gradients in the composite along the fiber-axis. The SFC was then furnace cooled to ambient temperature over a period of 4–5 h. The resulting matrix microstructure, which was highly consistent between samples, is shown in Fig. 1. The grain size immediately adjacent to the fibers was on the order of 15–25 μm, whereas the grain size further away from the fiber was about 25–40 μm.

Following fabrication, the SFC was sectioned into 0.0035 m thick disks perpendicular to the fiber-axis using a slow speed diamond wafering saw. The flat surfaces of each disk-shaped sample were polished to a 6 μm finish. The sample was then

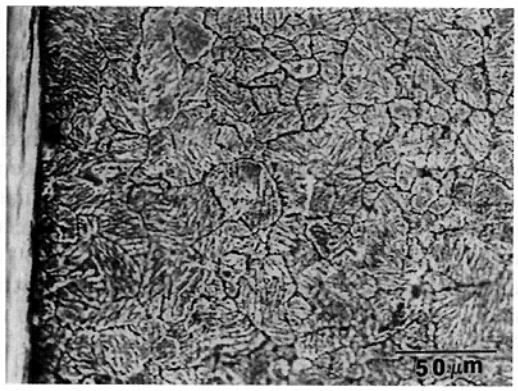

Fig. 1. Micrograph showing the matrix microstructure in the SFC system. The grain size is on the order of 15–25 μm near the interface (at left) and the far field grain size is on the order of 25–40 μm.

mounted on a specimen platform with a hole of 0.0015 m diameter (d_{hole}) such that the fiber was aligned exactly over the hole. A 0.002 m diameter tungsten indentor with a 0.00075 m diameter flat tip, connected to a servo-hydraulic MTS® frame equipped with an appropriate load cell ($\pm$0.1 N resolution) and displacement gauge ($\pm$0.2 μm resolution) was then utilized to apply a constant load to the top of the fiber and monitor the displacement of the fiber-top as a function of time. This arrangement allowed the interface to be loaded in shear. A schematic of the experimental approach is shown in Fig. 2. Although the tests were conducted under constant applied load, for small shear displacements of the fiber–matrix interface, the average interfacial shear stress, τ_{ave}, could be assumed to be approximately constant such that $\tau_{ave} \approx F/2\pi r_f t$, where F is the applied push-down load, r_f is the fiber radius and t is the specimen thickness. For elevated temperature tests, the indentor and the specimen platform, which were thermally isolated from the surrounding metallic fixtures by ceramic insulations, were heated independently using Kapton® insulated resistive tape heaters with platinum heating elements. This arrangement was capable of producing temperatures up to 400 K within a control band of $\pm$1 K. Prior to monitoring the creep response as outlined above, the critical shear stress required to debond (i.e. fracture) the interface (τ_d) was determined for each composite at various temperatures using constant displacement rate fiber push-out tests in conjunction with acoustic emission monitoring. All creep experiments were conducted at loads well under those required to cause interfacial debonding. Further details of the experimental procedure are given in Ref. [30].

Following both push-out and creep testing, the samples were inspected using scanning electron microscopy. Additionally, the top and bottom surface profiles of each of the as-crept samples were inspected using a Dektak 900 high resolution profilometer. The purpose of the profilometric examination was to distinguish between the contributions of interfacial sliding and any matrix creep (in the region immediately adjacent to the interface) to the overall fiber-top displacement measured in our experiments.

In order to obtain visual evidence of interfacial sliding, a Pb matrix composite reinforced with a continuous Ni or W plate was fabricated and sectioned to reveal a longitudinal section of the reinforcement. The section was metallographically polished, following which a pattern of ~25 μm square carbon grids was deposited on it. A schematic of this model composite is shown in Fig. 3. The sample was then mounted on a specimen platform with a rectangular slot (to allow the reinforcement to slide down relative to the matrix), and

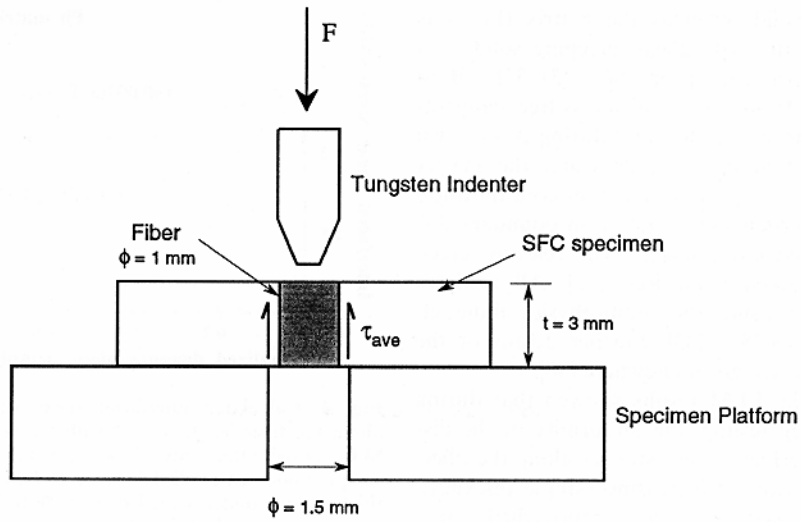

Fig. 2. Schematic representation of the experimental approach adopted in the single fiber push-down creep tests.

with the interfacial creep rate being significantly larger than the creep rate of the adjacent matrix. Clearly, the interface has its own deformation kinetics, separate from the deformation kinetics of the matrix.

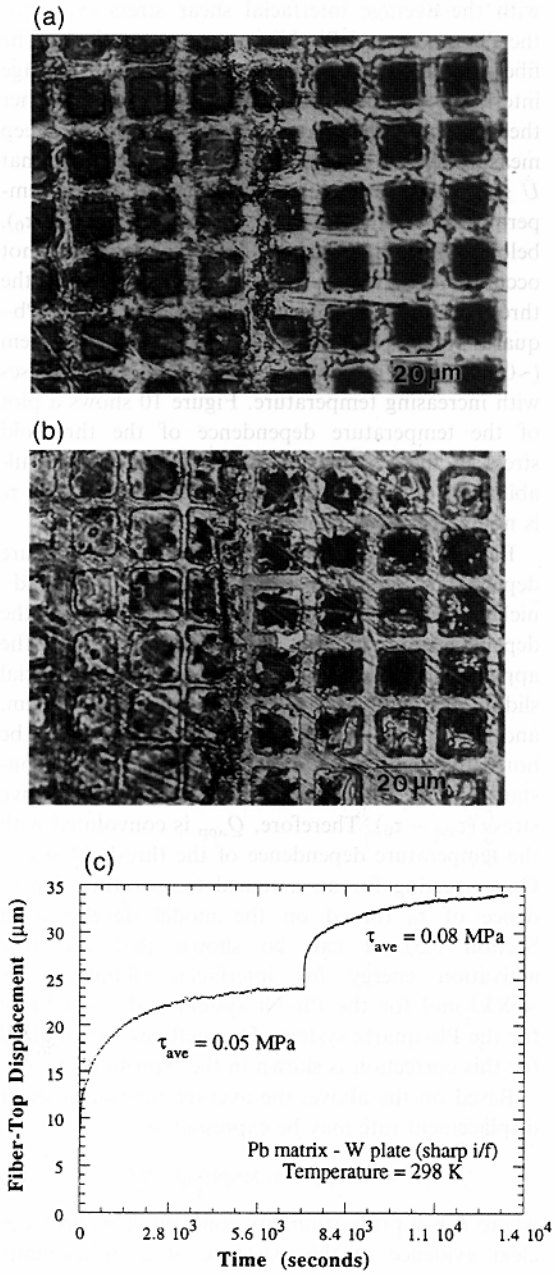

Fig. 5. (a) Optical micrograph showing the as-deposited carbon grid pattern across the reinforcement–matrix interface. There is perfect alignment of the grids on both sides of the interface. In the image, the lead matrix is on the left and the tungsten reinforcement is on the right. (b) Optical micrograph showing the appearance of the grid pattern in (a) following a stress change creep test. The deformation of the grid reveals a negligible matrix component and a sharp discontinuity at the interface. The matrix is on the left and the reinforcement is on the right. (c) Fiber-top displacement vs time plot obtained during the test to observe the interfacial sliding. As observed in (a) and (b) above, the entire observed time-dependent displacement is associated with interfacial sliding.

3.2. Creep response of the interface

Figures 6(a) and (b) show representative variations of fiber-top displacement as a function of creep time during push-down creep testing of the Pb–quartz and Pb–Ni systems, respectively. An apparent steady state is observed to be established within a relatively short time following loading the top of the fiber. This apparent steady state ensued for a considerable length of time (depending on the applied load and test temperature), before a tertiary stage was observed in some of the samples. The tertiary stage usually started once an appreciable fraction of the total fiber length emerged from the bottom surface, thereby causing τ_{ave} to increase significantly.

Figures 7(a) and (b) show an SEM macrograph and the surface profile of the top-face of a Pb–

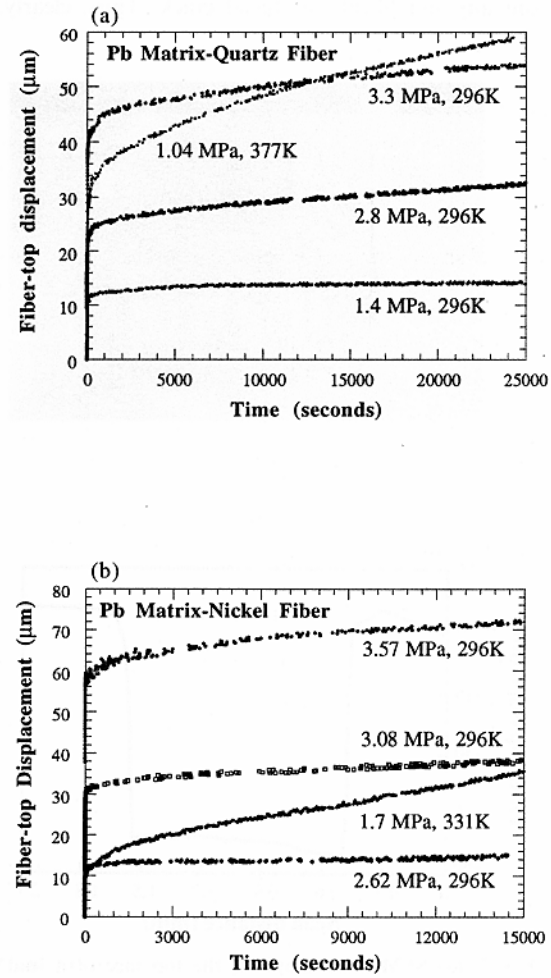

Fig. 6. Representative experimental creep responses of (a) the lead–quartz interface and (b) the lead–nickel interface at various applied interfacial shear stresses (τ_{ave}) and temperatures. In all cases, an initial transient followed by an apparent steady state is observed.

quartz SFC sample following a push-down creep test. The fiber is observed to have been slightly displaced inwards relative to the matrix, although no evidence of interfacial fracture is apparent. The downward displacement of the fiber-top is clearer in the profilometric scan in Fig. 7(b), which also shows that there is no associated downward displacement of the matrix immediately adjacent to the fiber. This verifies the premise that the entire time-dependent displacement noted in Fig. 6 is due to interfacial sliding, and not due to matrix creep.

Figures 8(a)–(c) show an SEM macrograph, and the top-face and bottom-face surface profiles, respectively, of a crept Pb–Ni SFC sample. Again, the fiber is observed to have been displaced downward in the absence of any interfacial fracture. The top-face profile shows this downward fiber displacement, and no apparent matrix creep adjacent to the fiber. Also, no interfacial crack is apparent in Fig. 8(b) around the fiber-top. The bottom-face profile shows the fiber protruding out, again without any significant interfacial crack. Thus, clearly,

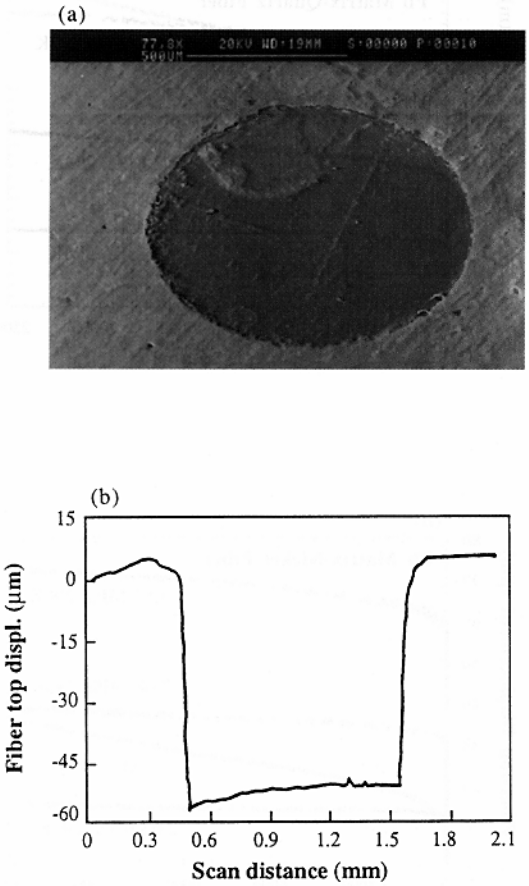

Fig. 7. (a) SEM macrograph of the top face of a lead–quartz SFC following push-down creep testing, showing that the fiber has been displaced downwards slightly relative to the matrix. No evidence of interfacial decohesion is observed. (b) Profilometric scan of the surface in (a), showing that the fiber has been displaced downwards, with no associated permanent matrix deformation.

in both the Pb–Ni and Pb–quartz systems, the interface slides by a creep mechanism.

Figures 9(a) and (b) show the variation of the apparent steady state fiber-top displacement rate with the average interfacial shear stress (τ_{ave}) for the Pb–quartz and Pb–Ni systems, respectively. The fiber-top displacement rate represents the average interfacial shear displacement rate ($\dot{U}$), since neither the fiber nor the matrix were observed to creep measurably, as discussed above. It is evident that $\dot{U}$ shows a linear dependence on τ_{ave} at all test temperatures. Further, a threshold shear stress (τ_0), below which interfacial sliding creep does not occur, is observed in both systems. At 296 K, the threshold stress is observed to be larger in the Pb–quartz system (~1.4 MPa) than in the Pb–Ni system (~0.7 MPa). Figure 9(a) shows that τ_0 decreases with increasing temperature. Figure 10 shows a plot of the temperature dependence of the threshold stress in the Pb–quartz system. Despite the availability of only three data points, it appears that τ_0 is nominally proportional to $1/T$.

Figures 11(a) and (b) show the temperature dependence of $\dot{U}$ in the lead–quartz and lead–nickel systems, respectively. In both cases, the dependence is of the Arrhenius type, with the apparent activation energy Q_{app} for interfacial sliding being 52 kJ/mol in the Pb–quartz system, and 66 kJ/mol in the Pb–Ni system. It is to be noted that Figs 11(a) and (b) are plotted for a constant applied stress τ_{ave}, and not constant effective stress ($\tau_{ave} - \tau_0$). Therefore, Q_{app} is convoluted with the temperature dependence of the threshold stress. On correcting for an assumed temperature dependence of τ_0 (based on the model developed in Section 3.3), it can be shown that the true activation energy for interfacial sliding Q_i is ~68 kJ/mol for the Pb–Ni system and ~62 kJ/mol for the Pb–quartz system. The methodology utilized for this correction is shown in the Appendix A.

Based on the above, the average interfacial shear displacement rate may be expressed as

$$\dot{U} = K(\tau_{ave} - \tau_0)\exp[-Q_i/RT] \qquad (1)$$

where K is a proportionality constant. This provides clear evidence of the existence of a diffusionally accommodated sliding process at the interface. The stress exponent of unity indicates that sliding occurs by diffusional creep. Such sliding, as discussed subsequently in Section 3.3, can occur either via matrix diffusion or via interfacial diffusion. The measured Q_i is much smaller than Q_{vol}. Also, as discussed in Section 3.3, matrix grain boundary diffusion is unlikely to play any role in interfacial sliding, since the average diffusion distance along the interface (determined by the spacing between interfacial asperities, λ) is expected to be much smaller than the matrix grain size d. Therefore, it appears that Q_i represents

quartz SFC sample following a push-down creep test. The fiber is observed to have been slightly displaced inwards relative to the matrix, although no evidence of interfacial fracture is apparent. The downward displacement of the fiber-top is clearer in the profilometric scan in Fig. 7(b), which also shows that there is no associated downward displacement of the matrix immediately adjacent to the fiber. This verifies the premise that the entire time-dependent displacement noted in Fig. 6 is due to interfacial sliding, and not due to matrix creep.

Figures 8(a)–(c) show an SEM macrograph, and the top-face and bottom-face surface profiles, respectively, of a crept Pb–Ni SFC sample. Again, the fiber is observed to have been displaced downward in the absence of any interfacial fracture. The top-face profile shows this downward fiber displacement, and no apparent matrix creep adjacent to the fiber. Also, no interfacial crack is apparent in Fig. 8(b) around the fiber-top. The bottom-face profile shows the fiber protruding out, again without any significant interfacial crack. Thus, clearly,

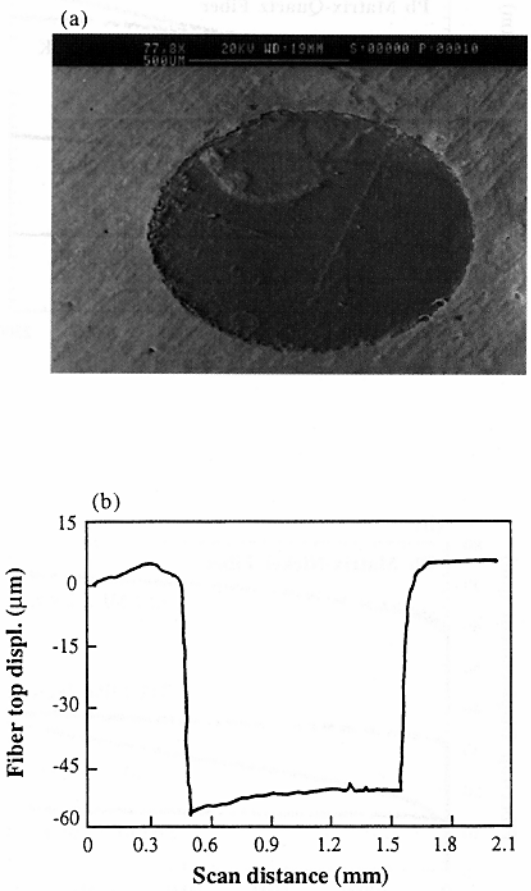

Fig. 7. (a) SEM macrograph of the top face of a lead–quartz SFC following push-down creep testing, showing that the fiber has been displaced downwards slightly relative to the matrix. No evidence of interfacial decohesion is observed. (b) Profilometric scan of the surface in (a), showing that the fiber has been displaced downwards, with no associated permanent matrix deformation.

in both the Pb–Ni and Pb–quartz systems, the interface slides by a creep mechanism.

Figures 9(a) and (b) show the variation of the apparent steady state fiber-top displacement rate with the average interfacial shear stress (τ_{ave}) for the Pb–quartz and Pb–Ni systems, respectively. The fiber-top displacement rate represents the average interfacial shear displacement rate ($\dot{U}$), since neither the fiber nor the matrix were observed to creep measurably, as discussed above. It is evident that $\dot{U}$ shows a linear dependence on τ_{ave} at all test temperatures. Further, a threshold shear stress (τ_0), below which interfacial sliding creep does not occur, is observed in both systems. At 296 K, the threshold stress is observed to be larger in the Pb–quartz system (~1.4 MPa) than in the Pb–Ni system (~0.7 MPa). Figure 9(a) shows that τ_0 decreases with increasing temperature. Figure 10 shows a plot of the temperature dependence of the threshold stress in the Pb–quartz system. Despite the availability of only three data points, it appears that τ_0 is nominally proportional to $1/T$.

Figures 11(a) and (b) show the temperature dependence of $\dot{U}$ in the lead–quartz and lead–nickel systems, respectively. In both cases, the dependence is of the Arrhenius type, with the apparent activation energy Q_{app} for interfacial sliding being 52 kJ/mol in the Pb–quartz system, and 66 kJ/mol in the Pb–Ni system. It is to be noted that Figs 11(a) and (b) are plotted for a constant applied stress τ_{ave}, and not constant effective stress ($\tau_{ave} - \tau_0$). Therefore, Q_{app} is convoluted with the temperature dependence of the threshold stress. On correcting for an assumed temperature dependence of τ_0 (based on the model developed in Section 3.3), it can be shown that the true activation energy for interfacial sliding Q_i is ~68 kJ/mol for the Pb–Ni system and ~62 kJ/mol for the Pb–quartz system. The methodology utilized for this correction is shown in the Appendix A.

Based on the above, the average interfacial shear displacement rate may be expressed as

$$\dot{U} = K(\tau_{ave} - \tau_0)\exp[-Q_i/RT] \qquad (1)$$

where K is a proportionality constant. This provides clear evidence of the existence of a diffusionally accommodated sliding process at the interface. The stress exponent of unity indicates that sliding occurs by diffusional creep. Such sliding, as discussed subsequently in Section 3.3, can occur either via matrix diffusion or via interfacial diffusion. The measured Q_i is much smaller than Q_{vol}. Also, as discussed in Section 3.3, matrix grain boundary diffusion is unlikely to play any role in interfacial sliding, since the average diffusion distance along the interface (determined by the spacing between interfacial asperities, λ) is expected to be much smaller than the matrix grain size d. Therefore, it appears that Q_i represents

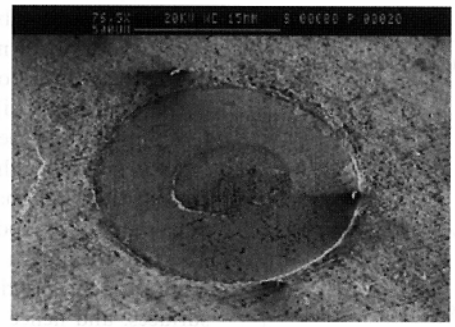

(a)

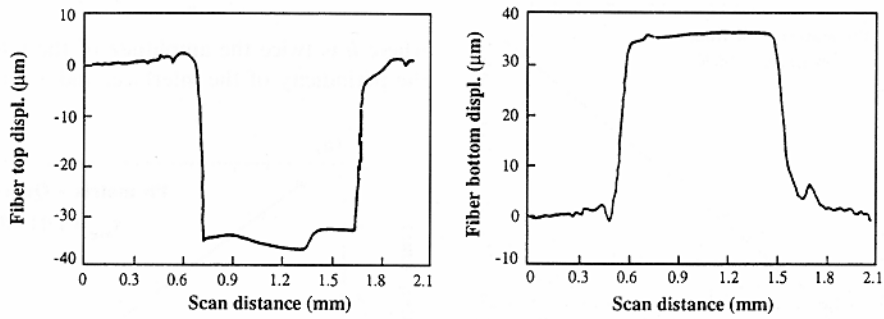

(b) (c)

Fig. 8. (a) SEM macrograph of the top face of a lead–nickel SFC following push-down creep testing, showing that the fiber has been displaced downwards slightly relative to the matrix. (b) Profilometric scan of the surface in (a), showing that the fiber has been displaced downwards, with no associated permanent matrix deformation. (c) Profilometric scan of the bottom surface of the same sample as in (b), showing that the fiber is protruding out of the matrix. There is no evidence of either top-face or bottom-face debonding of the fiber–matrix interface based on (b) and (c).

the activation energy for interfacial diffusion in the particular system.

In both lead–quartz and Pb–Ni systems, the corrected activation energy values (Q_i) are much smaller than that for volume self diffusion in lead ($Q_{vol} = 109$ kJ/mol). In the case of Pb–Ni, $Q_i \sim 68$ kJ/mol, which is close to the activation energy for grain boundary diffusion in lead ($Q_{gb} = 66$ kJ/mol). In the case of lead–quartz, $Q_i \sim 62$ kJ/mol, which is significantly less than Q_{gb}. This indicates that the interface in both cases acts as a *high diffusivity path*. In the case of lead–quartz, which has a sharp interface (lead and quartz have no mutual solubility), the interface behaves much like a free surface and displays a low activation energy, perhaps corresponding to that for surface diffusion. Contrarily, in Pb–Ni, where the interface is relatively diffuse, the activation energy for interfacial diffusion is close to Q_{gb}. In both cases, the mechanism of interfacial sliding appears to be interface-diffusion-controlled diffusional creep with a threshold stress (Bingham flow).

3.3. *Model for diffusion-controlled interfacial sliding*

In the following, a constitutive law for diffusion-controlled interfacial sliding is developed, based on the continuum grain boundary sliding model of Raj and Ashby [34]. The approach followed here is identical to that of Ref. [31] except in two respects. First, the present model incorporates the effect of a normal stress acting on the boundary, in addition to an applied shear stress. In a composite, this normal stress represents the radial stress (σ_R) acting on the interface and has two sources. The first, which is the dominant component, arises due to the difference between the coefficients of thermal expansion (CTE) of the matrix and the fiber. The second, typically smaller component results from differential lateral contraction of the fiber and matrix during axial deformation. The shear stress acting on the boundary represents the interfacial shear stress (τ_i) that is developed close to a fiber-end (either near a free surface, or at a break in the fiber) during axial deformation. In the context of the present exper-

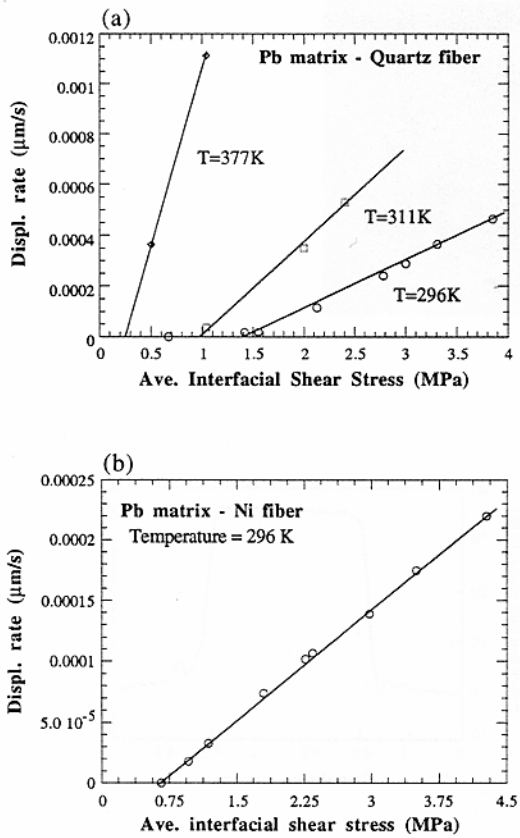

Fig. 9. Fiber-top displacement rate corresponding to the apparent steady state as a function of the applied average interfacial shear stress for (a) the lead–quartz SFC and (b) the lead–nickel SFC. A linear stress dependence of displacement rate at a constant temperature is observed in all cases. Additionally, a threshold stress, below which creep does not occur, is observed. In the case of lead–quartz (a), where data for several temperatures are available, the threshold stress is observed to decrease with increasing test temperature.

iments, τ_i is equal to the average shear stress τ_{ave} acting on the interface during push-down creep testing. Secondly, it is assumed here that the temperatures relevant for composite creep correspond to very low homologous temperatures for the fiber, and therefore the fiber does not participate in diffusional transport of matter. Therefore, in the present model, mass transport is assumed to occur (i) along the interface and (ii) through one side of the interface representing the matrix.

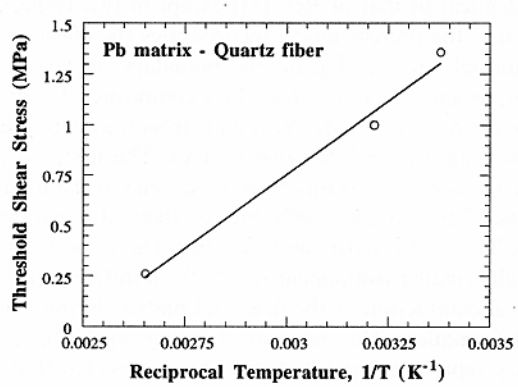

Fig. 10. Plot of the variation of the threshold stress (τ_0) in the lead–quartz SFC with temperature. τ_0 is observed to be inversely proportional to temperature (T).

As in Ref. [34], the boundary (in this case, representing the fiber–matrix interface) is considered to have a periodic topography, as shown in Fig. 12(a). This representation is particularly well suited to a reinforcement–matrix interface, since reinforcement surfaces, and hence the interface, are rarely, if ever, atomically smooth. For simplicity, the interfacial topography is assumed to have a cosine dependence on position, and is expressed as

$$x = \frac{h}{2}\cos\left(\frac{2\pi}{\lambda}y\right) \tag{2}$$

where h is twice the amplitude of the interface, λ is the periodicity of the interface, and x and y are the

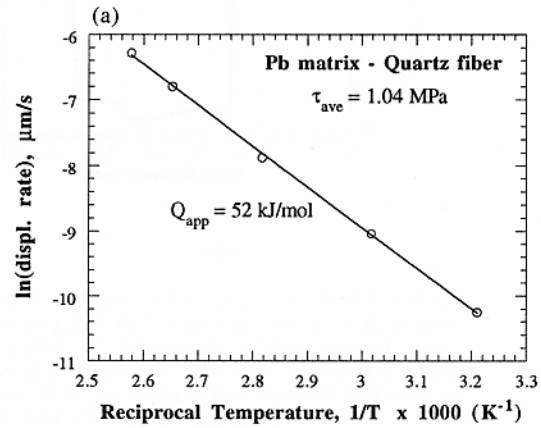

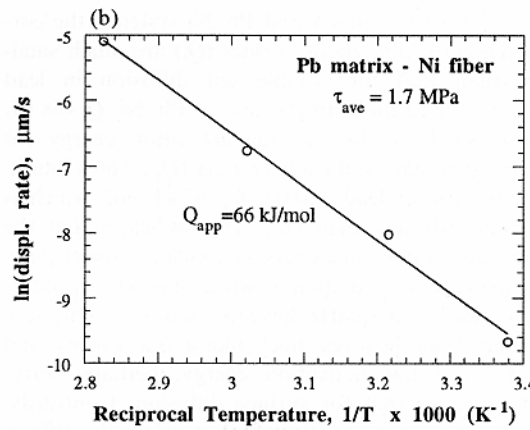

Fig. 11. Temperature dependence of the interfacial creep rate for (a) the lead–quartz SFC and (b) the lead–nickel SFC at a constant value of the applied average interfacial shear stress. The apparent activation energies computed from the plots are 52 and 66 kJ/mol for the lead–quartz and lead–nickel systems, respectively.

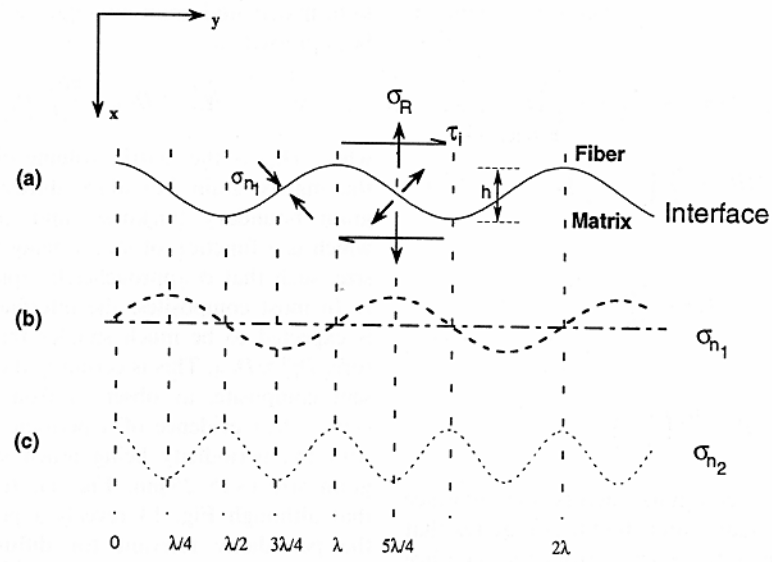

Fig. 12. Details of the periodic interface and the resulting normal stress distributions, as assumed in the model. (a) Idealized representation of the periodicity of the fiber–matrix interface along the fiber length. (b) Distribution of normal stress (σ_{n_1}) along the boundary due to an applied shear stress τ_i. (c) Distribution of normal stress (σ_{n_2}) along the boundary resulting from the presence of a normal (radial) residual stress σ_R. Note that the periodicity of σ_{n_2} is half that of σ_{n_1}.

coordinates normal to, and along the interface, respectively. In the context of a composite, x and y represent the radial and the axial fiber directions, respectively.

When a shear stress τ_i is applied on the interface, an instantaneous elastic accommodation occurs at the interface, resulting in a periodically varying normal stress along the interface, given by [34]

$$\sigma_{n_1} = \frac{\tau_i \lambda}{\pi h} \sin\left(\frac{2\pi}{\lambda} y\right) \tag{3}$$

where σ_{n_1} has the same periodicity as the interface. This is shown in Fig. 12(b), where σ_{n_1} is observed to vary from compressive through tensile values along the interface. It is this variation of the local normal stress at the boundary that is believed to drive boundary sliding through stress-assisted diffusional processes [34]. In a composite, an additional normal stress component is expected to be present due to the radial stress induced by differential thermal expansion/contraction and differential Poisson deformation of the fiber and matrix (e.g. Refs [35, 36]). Although the average radial stress in the matrix (σ_R) is independent of axial position along the interface, the periodicity of the interface introduces a periodicity in the normal stress acting on the interface. This may be expressed as

$$\sigma_{n_2} = \sigma_R \cos^2\theta \approx \frac{\sigma_R}{2}\left[\left(\frac{\pi h}{\lambda}\right)^2 \left\{\cos\left(\frac{4\pi}{\lambda} y\right) - 1\right\} + 2\right] \tag{4}$$

where θ, the local angular displacement of the boundary from the y-axis, is assumed to be small (or equivalently, the ratio $h/\lambda \gg 1$). This stress distribution is schematically shown in Fig. 12(c), where σ_{n_2} is observed to have half the periodicity of σ_{n_1}. Like σ_{n_1}, the y-position dependent σ_{n_2} contributes to mass transport along the interface by generating chemical potential gradients along the interface. Conservation of mass in the system requires that [34]

$$\nabla^2 \mu(x,y) = 0 \tag{5}$$

over all values of y and $0 \le x \le \infty$, where μ is the position-dependent chemical potential. The boundary conditions for solving the Laplacian in equation (5) are

$$\mu(0,y) = \mu_0 - \Omega(\sigma_{n_1}(y) + \sigma_{n_2}(y)) \tag{6a}$$

$$\mu(\infty,y) = \mu_0 - \Omega\sigma_R \tag{6b}$$

$$\frac{\partial \mu}{\partial y}\left(0, \frac{\lambda}{4}\right) = 0 \tag{6c}$$

$$\frac{\partial \mu}{\partial y}\left(0, \frac{5\lambda}{4}\right) = 0 \tag{6d}$$

where Ω is the atomic volume of the diffusing species (in this case, the matrix atoms), $x = \infty$ represents a distance sufficiently far away from the interface where the normal (radial) matrix stress equals its average value σ_R, and $y = \lambda/4$–$5\lambda/4$ represents a unit length comprising one period of the boundary over which mass is conserved. The sol-

ution of equation (5) with boundary conditions (6a)–(6d) yields

$$\mu(x,y) = \mu_0 - \Omega A \cos\frac{2\pi}{\lambda}\left(y - \frac{\lambda}{4}\right)e^{-2\pi x/\lambda} + \Omega B \cos\frac{4\pi}{\lambda}\left(y - \frac{\lambda}{4}\right)e^{-2\pi x/\lambda} \quad (7)$$

where

$$A = -\frac{\tau_i \lambda}{\pi h}$$

and

$$B = \frac{\sigma_R}{2}\left(\frac{\pi h}{\lambda}\right)^2.$$

Maintenance of continuity across the interface (i.e. between the matrix and the fiber) requires that the flux of matter into or away from the interface over any time increment Δt account precisely for the local displacement of the boundary along the y-direction. In a composite, matter may be transported between various locales along the interface (i) along the interface via interfacial diffusion and/or (ii) through the matrix side of the interface. This yields

$$\dot{\bar{U}} \sin\theta \cos\theta = -\Omega\left[J^x_m(0,y)\cos\theta + \delta_i \frac{\partial J^y_i}{\partial y}\right] \quad (8)$$

where $\dot{\bar{U}}$ is the average interfacial displacement rate, δ_i is the thickness of the interface, and J^x_m and J^y_i are the flux of matter through the matrix (locally normal to the interface) and along the interface, respectively. This is identical to the relationship continuity equaton in Ref. [34], except that in the present case, mass transport normal to the interface is allowed only along one side of the interface representing the matrix. Assuming that $h/\lambda \ll 1$ (i.e. $\theta \to 0$), equation (8) may be re-written as

$$J^x_m(0,y) - \delta_i \frac{\partial J^y_i}{\partial y} = \frac{dx}{dy}. \quad (9)$$

Substituting equation (7) in equation (9) and taking the solution at $y = n\lambda/4$, n being any odd integer, we obtain for the average interfacial shear displacement rate

$$\dot{\bar{U}} = \frac{2D^{eff}_m \Omega \lambda}{kT\pi h^2}\left[\tau_i + \sigma_R\left(\frac{\pi h}{\lambda}\right)^3\right] + \frac{4\delta_i D_i \Omega}{kTh^2}\left[\tau_i + 2\sigma_R\left(\frac{\pi h}{\lambda}\right)^3\right] \quad (10)$$

where D^{eff}_m and D_i are the effective matrix diffusivity and interface diffusivity, respectively. The first term in equation (10) represents the matrix contribution to interfacial sliding, whereas the second term represents the interface contribution. The effective matrix diffusivity D^{eff}_m incorporates the effects of both matrix and grain boundary diffusion, and may be expressed as

$$D^{eff}_m = D_{vol} + \frac{\pi\delta_{gb}}{d} D_{gb}\phi$$

where D_{vol} is the matrix volume diffusivity, D_{gb} is the matrix grain boundary diffusivity, δ_{gb} is the grain boundary thickness, and ϕ is a constant which is a function of d/λ, d being the matrix grain size, such that ϕ approaches 0 rapidly as d exceeds λ. In most composites, the interfacial periodicity λ is expected to be much smaller than d, and therefore, $D^{eff}_m \approx D_{vol}$. This is certainly the case in the present composite, as observed from Fig. 13, which shows clear evidence of a periodic Pb–Ni interface with the periodicity being much smaller than the grain size (~15–25 μm, Fig. 1). It is to be noted that although Fig. 13 reveals a periodic interface, the periodicity relevant for diffusional transport necessary for interfacial sliding is expected to be of a finer scale than that revealed by the micrograph, and therefore, λ cannot be obtained directly from the photograph. In composites where the activation energy for interfacial diffusion is substantially smaller than that for matrix volume diffusion, as is the case in the present experimental systems (both Pb–Ni and Pb–quartz), the second term in equation (10) is expected to dominate. Therefore, equation (10) may be re-written as

$$\dot{\bar{U}} \approx \frac{4\delta_i D_i \Omega}{kTh^2}\left[\tau_i + 2\sigma_R\left(\frac{\pi h}{\lambda}\right)^3\right] \quad (11)$$

yielding an interfacial shear strain rate of

$$\dot{\gamma} \approx \frac{4\delta_i D_i \Omega}{kTh^3}\left[\tau_i + 2\sigma_R\left(\frac{\pi h}{\lambda}\right)^3\right]. \quad (12)$$

Comparing equation (11) with the experimentally obtained equation (1), it is apparent that they are identical, with the pre-exponential constant K and the threshold stress τ_0 in equation (1) being

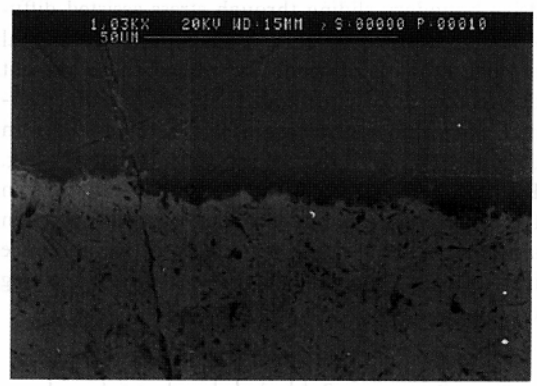

Fig. 13. SEM micrograph of a representative region of the interface in a Pb–Ni SFC, clearly revealing its periodic nature. Different scales of periodicity may be observed, depending on the magnification.

given by

$$K = \frac{4\delta_i D_{i0}\Omega}{kTh^2} \tag{13}$$

and

$$\tau_0 = -2\sigma_R\left(\frac{\pi h}{\lambda}\right)^3 \tag{14}$$

where D_{i0} is the frequency factor for interfacial diffusion, and σ_R in most metal–matrix composites is a compressive (and hence negative) stress. Clearly, the threshold stress observed in the experiments arises from the residual radial compressive stresses acting at the fiber–matrix interface, and is related to the geometry of the interface.

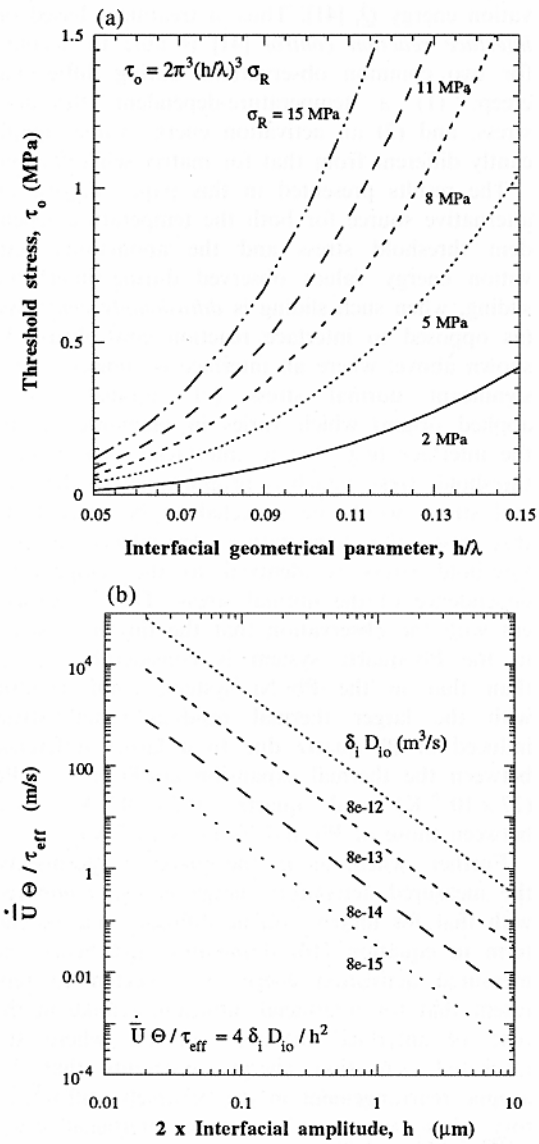

Fig. 14. (a) Calculated variation of the threshold stress τ_0 with the interfacial geometrical parameter, h/λ, for various values of the residual radial stress σ_R. Here h is twice the interfacial amplitude, and λ is the periodicity of the interface. (b) Variation of the parameter $\dot{\bar{U}}\Theta/(\tau_i - \tau_0)$ with h for various values of $\delta_i D_{i0}$.

Figure 14(a) shows a plot of τ_0 vs h/λ for different values of the radial compressive stress σ_R. Using this plot, the h/λ ratio for a given interface may be obtained once τ_0 is known. From finite element modeling, σ_R was estimated to be about 8 MPa in the Pb–Ni SFC at 298 K. Finite element analysis showed that σ_R predominantly constitutes the thermal residual stress component, and changes very little upon the application of an indentation (or push-down) stress to the top of the fiber. This is in agreement with finite element results obtained by Ghosn *et al.* [37] in SiC–Ti composites. Based on the measured τ_0 value of 0.7 MPa at 296 K, and taking $\sigma_R = 8$ MPa, we obtain $h/\lambda \approx 0.11$ for the interface in the Pb–Ni SFC. Equation (11) may be re-written as

$$\frac{\dot{\bar{U}}}{\tau_{eff}}\Theta = \frac{4\delta_i D_{i0}}{h^2} \tag{15}$$

where $\Theta = (kT/\Omega)e^{Q_i/RT}$ is a temperature-dependent constant, $4\delta_i D_{i0}/h^2$ is a temperature-independent constant, τ_{eff} is the effective shear stress acting on the interface ($\tau_{eff} = \tau_i - \tau_0$), and $\dot{\bar{U}}$ is the average interfacial shear displacement rate (or fiber-top displacement rate). The quantities on the left-hand side of equation (15) are experimentally determinable. Therefore, although it is not possible to independently determine the interfacial width h and the pre-exponential $\delta_i D_{i0}$, equation (15) may be utilized to determine the ratio $4\delta_i D_{i0}/h^2$ from experiments. Figure 14(b), which shows a plot of $\dot{\bar{U}}\Theta/(\tau_i - \tau_0)$ vs h at various values of $\delta_i D_{i0}$, can be used to estimate h and $\delta_i D_{i0}$. For instance, using the ambient temperature experimental values of $\dot{\bar{U}} = 0.0001$ μm/s at $\tau_i = 2.25$ MPa, $\tau_0 = 0.7$ MPa, and $Q_i = 68$ kJ/mol, one obtains a $\delta_i D_{i0}$ value close to 8×10^{-12} m^3/s (~100 times the grain boundary diffusion pre-exponential $\delta_{gb} D_{gb}$ for Pb) at $h = 0.1$ μm. Although the exact values of h and h/λ are difficult to ascertain by microscopic examination, it is apparent from the geometry of the interface in Fig. 13 that h/λ and h values of 0.11 and 0.1 μm, respectively (where h and λ are the height and spacing of interfacial asperities, respectively), are not unreasonable. Where more accurate values of h are available, Fig. 14(b) may be utilized to accurately determine the interface diffusion pre-exponential $\delta_i D_{i0}$ based on fiber push-down creep data.

4. DISCUSSION

It is evident from the above results that bi-material interfaces, just like grain boundaries, are capable of sliding by diffusional creep. When a normal compressive stress is associated with the interface, a threshold stress below which interfacial sliding does not occur, is expected. Composites,

multi-layered materials and film–substrate systems are examples of systems with bi-material interfaces where shear as well as normal stresses may arise in service. Therefore, such interfaces are expected to slide following the constitutive creep law developed above. It is important to note that this type of diffusionally accommodated sliding occurs even in well-bonded interfaces, and is fundamentally different from frictionally controlled sliding which has been observed in many composites with debonded or weak (i.e. easily fractured) interfaces (e.g. Refs [24, 37–39]).

From the data reported above, three key points emerge. First, a continuum model seems to be adequate to describe interfacial sliding, at least in the present experimental systems. Secondly, the threshold stress appears to originate predominantly from the radial stresses acting on the interface. And finally, the measured activation energy for interfacial sliding is quite low relative to the activation energy of volume diffusion in Pb.

As seen in equation (10), interfacial sliding may be governed by diffusion through both the matrix and the interface. When interfacial diffusivity is high compared to matrix diffusivity, the second term in equation (10) should dominate. Otherwise both terms have to be taken into account. Both matrix-diffusion-driven and the interface-diffusion-driven components are influenced by the presence of a normal interfacial stress. When the normal stress is tensile, this leads to a larger effective shear stress at the interface, and hence a larger creep/sliding rate. When the normal stress is compressive, as is the case in most metal–matrix composites, this results in a threshold stress below which creep cannot occur.

Indirect evidence of diffusionally accommodated sliding at phase boundaries and interfaces during creep/superplastic deformation has been obtained in many material systems, including dispersion strengthened metals (e.g. [40–43]), eutectic alloys [44] and discontinuously reinforced metal–matrix composites [19, 27, 45–47]. The inferred kinetics of interfacial sliding in these systems vary considerably. In most cases, interface sliding controlled creep results in a stress exponent (n) ranging from 1 to 2 [41, 44], shows a temperature dependent threshold stress below which creep does not occur [41], and displays an activation energy which is typically well over that for matrix volume diffusion Q_{vol} (e.g. Refs [41, 43, 46]), but is sometimes below Q_{vol} [44].

It is generally accepted that grain boundary sliding (or, as in our case, interface sliding) may be represented by a continuum model of diffusional creep (e.g. Ref. [34]) when the boundary (or interface) has an abundant population of mobile grain boundary dislocations (GBDs) which allow the boundary to act as a perfect source and sink of vacancies [41]. When either the density or the mobility of dislocation sources in the boundary is limited, however, the kinetics of boundary/interface sliding is believed to become "interface reaction controlled" [41]. Such interface reaction control may arise from the interaction of GBDs or interface dislocations (IDs) with interfacial dispersoids or asperities, which exert a drag on mobile GBDs/IDs, resulting in a threshold stress for creep. When the mobility of GBDs/IDs is high, a threshold stress would be the only manifestation of interface reaction control. But when the mobility of GBDs/IDs is restricted (e.g. due to the difficulty of rearranging atoms on the more refractory/stiffer side of the interface), interface reaction control may also result in a high activation energy Q_i [41]. Thus, a treatment based on *interface reaction control* [41] is able to account for two common observations during diffusional creep: (1) a temperature-dependent threshold stress, and (2) an activation energy value significantly different from that for matrix self diffusion.

The results presented in this paper suggest an alternative source for both the temperature-dependent threshold stress and the anomalous activation energy values observed during interfacial sliding, when such sliding is *diffusionally controlled* (as opposed to interface reaction controlled). As shown above, where an interface is subjected to a significant normal stress (of residual and/or applied origin) which varies in magnitude along the interface (e.g. due to interfacial asperities), a threshold stress, which is proportional to the normal stress, would be expected to be present. In this case, the temperature dependence of the threshold stress is identical to the temperature dependence of the normal stress. This is consistent with the observation that the threshold stress in the Pb–quartz system is considerably larger than that in the Pb–Ni system, commensurate with the larger thermal residual radial stress induced in Pb–quartz due to a larger difference between the thermal expansion coefficients of Pb (27×10^{-6}/K) and quartz (0.5×10^{-6}/K) than between those of Pb and Ni (15×10^{-6}/K).

Further, when, as in the present experiments, the measured activation energy is low compared with that for matrix volume diffusion, the second term in equation (10) dominates, and hence the measured activation energy is expected to represent that for interfacial diffusion. Unlike in the case of interface reaction control, where the measured activation energy represents that for atomic rearrangement in the relatively stiff/refractory phase (necessary to move interfacial dislocations and thereby create vacancies), under diffusion control, the measured activation energy simply represents that for atomic diffusion along the interface, which is a high diffusivity path. Therefore, when vacancies are in plentiful supply, *interface diffusion control is likely to result in a*

low Q_i, rather than the high Q_i values typically observed under interface reaction control. Indeed, Nimmagadda and Sofronis [47] calculated the interfacial diffusion coefficient based on the creep data of Rosler and co-workers [19, 48], and concluded that the activation energy for interfacial diffusion in TiAl–Ti_2AlC composites is significantly lower than that for volume diffusion in the matrix. Depending on the diffusing species, the measured Q-value may be lower than that for matrix volume diffusion even when sliding is interface reaction controlled. This was noted by Ignat and Bonnet [44], who found that dislocation movement along interlamellar interfaces in the Al–$CuAl_2$ eutectic is controlled by interfacial diffusion of Cu. In the present experiments, the corrected activation energy value for interfacial sliding in the Pb–Ni system is close to, but somewhat higher than that for grain boundary self diffusion in Pb. This is similar to the finding of Ref. [47], where the activation energy for interfacial diffusion was found to lie between those for volume and grain boundary diffusion. Since Ni has negligible solubility in Pb, and since the tracer diffusivity of Ni in Pb (~44 kJ/mol, Ref. [49]) is much lower than the corrected Q_i value, it is inferred that Q_i represents the activation energy for diffusion of Pb along the Pb–Ni interface.† In the case of Pb–quartz, the corrected Q_i is ~62 kJ/mol. The interface is sharp because of the absence of mutual solubility, and quartz being largely covalent, is unlikely to dissociate and contribute Si^{4+} for diffusion along the interface. Therefore, in this case too, Q_i is thought to represent the activation energy for Pb diffusion along the interface. Because of the absence of mutual solubility between Pb and quartz, the sharp Pb–quartz interface appears to be a higher diffusivity path than the Pb–Ni interface, which is comparatively diffuse in character.

Since the activation energy values observed here are consistent with those for interfacial diffusion (and not the anomalously high values expected when vacancies have to be created via dislocation motion [41]), it seems that the interfaces for both model composites have adequate sources and sinks of vacancies. Interfacial sliding in both cases is therefore diffusionally controlled, allowing the use of a continuum approach. Significantly, the continuum approach is able to account for the presence of a temperature-dependent threshold stress which is frequently encountered in diffusional creep, but has so far been explicable only by invoking an interface-controlled mechanism. This approach is clearly attractive in situations where (1) an abundant supply of vacancy sources and sinks are available at the interface, and (2) when significant residual stresses (which result in normal interfacial stresses) exist in the material. Indeed, much of the early observations of threshold stresses in diffusional creep were in dispersion strengthened systems containing a ceramic dispersoid in a metallic matrix (e.g. Refs [40, 42]), where substantial differences in the coefficients of thermal expansion (and therefore large residual stresses) are expected between the constituent phases. The present work suggests that such internal residual stresses may lead to threshold effects even under diffusion control.

Although in the present work, the measured Q_i values were found to be low, it is possible to obtain anomalously high activation energy values even when vacancies are readily available for sliding to be diffusionally controlled. Equation (10) may be re-written in the form

$$\dot{U} = K_1[\tau_i - \tau_{th}]\exp\left[-\frac{Q_m^{eff}}{RT}\right] + K_2[\tau_i - 2\tau_{th}]\exp\left[-\frac{Q_i}{RT}\right] \quad (16)$$

where K_1 and K_2 are appropriate constants, $\tau_{th} = \sigma_R(\pi h/\lambda)^3$, and as discussed before, $Q_m^{eff} \approx Q_{vol}$ when the interfacial periodicity λ is less than the grain size d. Taking the first derivative of $\ln \dot{U}$ with respect to $1/T$, we obtain

$$\frac{\partial \ln \dot{U}}{\partial(1/T)} = -\frac{\partial \tau_{th}}{\partial(1/T)}\left[\frac{1}{\tau_i - \tau_{th}} + \frac{1}{\tau_i - 2\tau_{th}}\right] - \left(\frac{Q_{vol} + Q_i}{R}\right) \quad (17)$$

Thus, when the contributions of matrix and interface diffusion are of comparable magnitudes, the apparent activation energy Q_{app} obtained by plotting $\ln \dot{U}$ vs $1/T$ at a constant applied τ_i is larger than Q_{vol}, even if τ_{th} is not temperature dependent. In general, τ_{th} is related to σ_R, which is temperature dependent, and therefore, the activation energy value obtained from a $\ln \dot{U}$ vs $1/T$ plot is likely to be anomalously large. Additionally, in composites or multi-phase alloys, the stiffness difference between the constituent phases is likely to have some contribution to σ_R, making τ_{th} dependent on the applied stress, and possibly altering the stress dependence of $\dot{U}$.

Thus, the results presented here suggest the means to rationalize some of the observations associated with diffusional creep in multi-phase systems based on a continuum approach. Significantly, the present experiments allow studying the creep behavior of the interface in isolation from the rest of the system, and therefore, are believed to be more closely representative of the interface *per se*

†Although Pb has limited solubility in Ni, the tracer diffusivities of all elements in Ni are very low (activation energies are well upwards of 100 kJ/mol [49]), and therefore Q_i cannot represent diffusion of Pb in Ni.

than data available hitherto. Clearly, additional work is necessary before it can be established whether the proposed mechanism is capable of capturing the principal characteristics of diffusional flow in complete systems, when such flow is controlled by interfacial sliding.

5. CONCLUSIONS

The interfacial creep characteristics in model single fiber composite systems with two different types of interface (sharp and diffuse) were studied using a single fiber push-down approach. When the elastic modulus of the fiber is much larger than that of the matrix, this set up results in a nearly constant interfacial shear stress along the specimen thickness, provided: (1) the sample is thick relative to the fiber diameter, and (2) the opening in the base plate is only slightly larger than the fiber diameter. Use of this experimental approach allowed isolation of the interfacial creep response, without the convoluting effects of associated matrix deformation.

Both types of interface were found to display diffusional creep ($n = 1$), with a threshold stress that decreases with increasing temperature. The activation energy associated with interfacial sliding was found to be close to or less than that for grain boundary diffusion in the lead matrix. High resolution profilometry as well as microscopic observation of the matrix region immediately adjacent to the interface suggested that most (if not all) permanent deformation was associated with interfacial sliding, rather than matrix deformation. This, coupled with the low measured activation energy values, suggested that interfacial creep in the present experimental systems is *interface diffusion controlled*.

A continuum model was utilized to account for the effect of normal interfacial stresses (due to thermal residual stresses and/or Poisson effect) on the kinetics of diffusion-controlled interface sliding. The model showed that both matrix and interfacial diffusion may contribute to interfacial creep, the stress dependence of strain rate due to both matrix and interface diffusion being linear. Furthermore, in both cases, the effective interfacial shear stress is reduced by a threshold stress which is directly related to the normal/radial compressive stress acting on the interface, as well as the interfacial topography. When interfacial diffusion is rapid compared to matrix diffusion, the measured activation energy for interfacial creep represents that for interfacial diffusion, as in the present experiments. When the matrix and interface diffusion contributions are comparable, the apparent activation energy value obtained by plotting ln(displacement rate) against $1/T$ is expected to be anomalously high.

The experimental results were found to be in qualitative agreement with the model. Based on the model and experiments, it is hereby proposed that fiber–matrix interfaces undergo thermally activated sliding via *diffusion-controlled* diffusional creep. Significantly, all experimental observations, including the temperature-dependent threshold stress and the observed activation energy values, may be adequately explained using this model, without invoking interface reaction control of diffusional creep.

Acknowledgements—This work was supported by the National Science Foundation, Division of Materials Research, under contract number DMR-9423668. The authors wish to thank B. S. Majumdar for the high resolution profilometry results and A. Gopinath for his assistance with the solution of the differential equation. The many insightful discussions with T. R. McNelley are gratefully acknowledged. Thanks are also due to R. Nagarajan for SEM characterization of the interface.

REFERENCES

1. Jech, R. W. and Weber, E. P., Clevite Research Centre Final Report No. 55-953-C.
2. Dean, A. V., *J. Inst. Metals*, 1967, **95**, 79.
3. Ellison, E. G. and Harris, B., *Appl. Mater. Res.*, 1966, **5**, 33.
4. Kelly, A. and Tyson, W. R., *J. Mech. Phys. Solids*, 1965, **13**, 329.
5. Kelly, A. and Tyson, W. R., *J. Mech. Phys. Solids*, 1966, **14**, 177.
6. De Silva, A. R. T., *J. Mech. Phys. Solids*, 1968, **16**, 169.
7. Doruk, M. and Yue, A. S., *Metall. Trans. A*, 1976, **7A**, 1465.
8. Mclean, M., *Proc. RISO Int. Symp. on Fatigue and Creep of Composite Materials*, 1982, p. 77.
9. Mclean, M., *Compos. Sci. Technol.*, 1985, **23**, 37.
10. Matsuura, K., Chou, M. and Matsuda, N., *Mater. Trans., JIM*, 1991, **32**, 1062.
11. Weber, C. H., Yang, J. Y., Lofvander, P. A., Levi, C. G. and Evans, A. G., *Acta metall. mater.*, 1993, **41**, 2681.
12. Dragone, T. L., Schlautman, J. J. and Nix, W. D., *Metall. Trans. A*, 1991, **22A**, 1029.
13. Dlouhy, A., Merk, N. and Eggeler, G., *Acta metall. mater.*, 1993, **41**, 3245.
14. Dlouhy, A., Eggeler, G. and Merk, N., *Acta metall. mater.*, 1995, **43**, 535.
15. Schwenker, S. W. and Eylon, D., *Metall. Mater. Trans. A*, 1996, **27A**, 4193.
16. Kelly, A. and Street, K. N., *Proc. R. Soc. Lond. A*, 1972, **328**, 2073.
17. Bullock, E., Mclean, M. and Miles, D. E., *Acta metall.*, 1977, **25**, 333.
18. Goto, S. and Mclean, M., *Acta metall. mater.*, 1991, **39**, 153.
19. Rosler, J., Bao, G. and Evans, A. G., *Acta metall. mater.*, 1991, **39**, 2733.
20. Kim, K. T. and McMeeking, R. M., *Mech. Mater.*, 1995, **20**, 153.
21. Nimmagadda, P. B. R. and Sofronis, P., *Mech. Mater.*, 1996, **23**, 1.
22. Yoda, S., Kurihara, N., Wakashima, K. and Umekawa, S., *Metall. Trans. A*, 1978, **9A**, 1229.
23. Dutta, I., Mitra, S. and Wiest, A. D., in *Residual Stresses in Composites*, ed. E. V. Barrera and I. Dutta. TMS–AIME, Warrendale, Pennsylvania, 1993, pp. 273–292.
24. Mitra, S., Dutta, I. and Hansen, R. C., *J. Mater. Sci.*, 1991, **26**, 6223.

25. Furness, J. A. G. and Clyne, T. W., *Mater. Sci. Engng*, 1991, **A141**, 199.
26. Cox, B. N., *Acta metall. mater.*, 1990, **38**, 2411.
27. Rosler, J., Valencia, J. J., Levi, C. G., Evans, A. G. and Mehrabian, R., *Mater. Res. Soc. Proc.*, 1990, **194**, 241.
28. Sofronis, P. and McMeeking, R. M., *Mech. Mater.*, 1992, **18**, 55.
29. Massalski, T. B. (ed.), *Binary Alloy Phase Diagrams*. ASM International, Metals Park, Ohio, 1990, pp. 2837–2838.
30. Funn, J. V., *Creep behavior of the interface region in continuous fiber reinforced metal–matrix composites*. M.S. thesis, Naval Postgraduate School, Monterey, California, 1997.
31. *ASM Metals Handbook*, Vol. 2, 10th edn. ASM International, Metals Park, Ohio, 1990.
32. Frost, H. J. and Ashby, M. F., *Deformation Mechanism Maps, the Plasticity and Creep of Metals and Ceramics*. Pergamon Press, Oxford, 1982.
33. ANSYS Release 5.3, Users Manual, ANSYS Inc., Houston, Pennsylvania, 1994.
34. Raj, R. and Ashby, M. F., *Metall. Trans.*, 1971, **2**, 1113.
35. Chawla, K. K., *Composite Materials: Science and Engineering*. Springer, New York, 1987.
36. Clyne, T. W. and Withers, P. J., in *An Introduction to Metal Matrix Composites*, ed. E. A. Davis and I. M. Ward. Cambridge University Press, Cambridge, 1993.
37. Ghosn, L. J., Eldridge, J. I. and Kantzos, P., *Acta metall. mater.*, 1994, **42**, 3895.
38. Watson, M. C. and Clyne, T. W., *Acta metall. mater.*, 1992, **40**, 141.
39. Parthasarathy, T. A., Barlage, D. R., Jero, P. D. and Kerans, R. J., *J. Am. Ceram. Soc.*, 1994, **77**, 3232.
40. Ashby, M. F., *Scripta metall.*, 1969, **3**, 837.
41. Arzt, E., Ashby, M. F. and Verall, R. A., *Acta metall.*, **31**, 1977.
42. Sautter, F. K. and Chen, E. S., *Proc. 2nd Bolton Landing Conf. on Oxide Disperison Strengthening*. Gordon & Breach, New York, 1969, p. 495.
43. Stang, R. G. and Barret, C. R., *Scripta metall.*, 1973, **7**, 233.
44. Ignat, M. and Bonnet, R., *Acta metall.*, 1983, **31**, 1991.
45. Mishra, R. S. and Mukherjee, A. K., *Scripta metall. mater.*, 1991, **25**, 271.
46. Mishra, R. S., Bieler, T. R. and Mukherjee, A. K., *Acta metall. mater.*, 1997, **45**, 561.
47. Nimmagadda, P. B. R. and Sofronis, P., *Acta mater.*, 1996, **44**, 2711.
48. Rosler, J. and Evans, A. G., *Mater. Sci. Engng*, 1992, **A153**, 438.
49. Brandes, E. A. and Brook, G. B. (ed.), *Smithells Metals Reference Book*, 7th edn. Butterworth-Heinemann, Oxford, 1992.

APPENDIX A

Effect of temperature dependence of τ_0 on measured Q

The experimentally obtained form of the interfacial shear displacement rate is

$$\dot{U} = K(\tau_i - \tau_0)\exp[-Q_i/RT] \tag{A1}$$

where τ_i is the applied interfacial shear stress. Taking the first derivative of $\ln \dot{U}$ with respect to $1/T$, we obtain

$$\frac{\partial \ln \dot{U}}{\partial(1/T)} = -\frac{\partial \ln(\tau_i - \tau_0)}{\partial(1/T)} - \left(\frac{Q_i}{R}\right) = -\frac{Q_{app}}{R} \tag{A2}$$

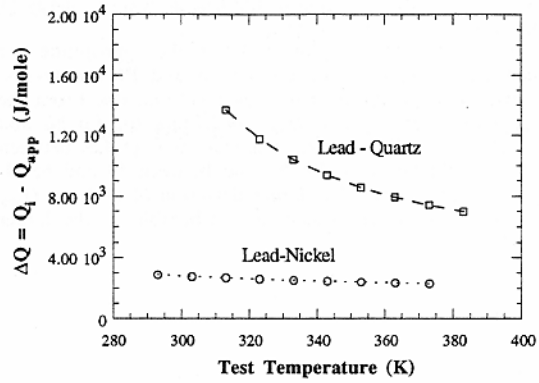

Fig. 15. Deviation of the true activation energy Q_i from the measured activation energy Q_{app} within appropriate test temperature regimes for Pb–Ni and Pb–quartz. This deviation is due to the temperature dependence of the threshold stress τ_0.

where Q_{app} is the experimentally measured apparent activation energy, and Q_i is the true activation energy. Therefore

$$-\left[\frac{Q_{app} - Q_i}{R}\right] = \frac{\partial \ln(\tau_i - \tau_0)}{\partial(1/T)} = \frac{1}{\tau_i - \tau_0}\frac{\partial(\tau_i - \tau_0)}{\partial(1/T)} = -\frac{1}{\tau_i - \tau_0}\frac{\partial \tau_0}{\partial(1/T)} \tag{A3}$$

at constant τ_i.

Based on the analysis in Section 3.3, the threshold shear stress τ_0 may be represented as [equation (14)]

$$\tau_0 = 2\sigma_R\left(\frac{\pi h}{\lambda}\right)^3 \tag{A4}$$

where σ_R is the radial compressive stress acting on the fiber–matrix interface (primarily of thermal residual origin), and h and λ are twice the amplitude and periodicity of the interface, respectively. The temperature dependence of τ_0 thus arises from that of the residual radial stress σ_R. Since τ_0 is observed to vary linearly with $1/T$ (Fig. 10), σ_R may be represented as

$$\sigma_R = \sigma_{R0}\left(\frac{A}{T} + B\right) \tag{A5}$$

where σ_{R0} is the value of the radial residual stress at ambient temperature, and A and B are constants. The constants A and B may be estimated using the following boundary conditions:

$$\sigma_R = \sigma_{R0} \text{ at } T = 300\text{ K} \text{ and } \sigma_R = 0 \text{ at } T = 523\text{ K}. \tag{A6}$$

Based on finite element analysis, the radial residual stresses induced at the Pb–Ni and Pb–quartz interfaces during cooling from an assumed fabrication temperature of 543–300 K were computed to be about 8 and 10 MPa, respectively. Combining equations (A4), (A5) and (A6), and assuming that $h/\lambda \approx 0.1$ [reasonable for both systems according to Fig. 14(a)], we obtain

$$\tau_0 = C\left(\frac{704}{T} + 1.3\right) \tag{A7}$$

where $C = 0.5$ for Pb–Ni and $C = 0.6$ for Pb–quartz. Substituting equation (A7) in equation (A3) yields

$$\Delta Q = Q_i - Q_{app} = R\left[\frac{\tau_i}{704C} - \frac{1}{T} + \frac{1}{704}\right]^{-1} \tag{A8}$$

where ΔQ is the deviation of the true activation energy Q_i from the measured value Q_{app}.

Figure 15 shows a plot of ΔQ in the appropriate test temperature regimes for the Pb–Ni and Pb–quartz systems, based on the data in Figs 11(a) and (b). From the magnitudes of ΔQ and Q_{app} (66 kJ/mol for Pb–Ni and 52 kJ/mol for Pb–quartz), it is clear that Q_i lies between 68 and 69 kJ/mol for Pb–Ni and between 59 and 65 kJ/mol for Pb–quartz. The larger deviation of Q_i from Q_{app} for the lead–quartz system is attributable to the larger thermal residual stress present in lead–quartz at ambient temperature, which in turn leads to a stronger temperature dependence of the radial stress (and therefore the threshold stress). Clearly, relatively little error is associated with the determination of Q_i in Pb–Ni, and Q_i can be taken to be 68 kJ/mol. In Pb–quartz, because of the higher thermal expansion mismatch, and hence the larger temperature dependence of residual stress, the error is larger, with the mean Q_i for the lead–quartz interface being about 62 kJ/mol.